Check for updates

CHEMICAL PHYSICS

Bioinspired single-shot polarization photodetector based on four-directional grating arrays capped perovskite single-crystal thin film

Wenzhong Fang[1,2]†, Chengben Liu[1,3]†, Zixin Zhu[1]†, Chao Wu[4]†, Qunfeng Cheng[3]†, Qian Song[5], Yang Wang[5], Xintao Lai[5], Yanlin Song[5], Lei Jiang[1], Mingzhu Li[1,6]*

Copyright © 2024 The Authors, some rights reserved; exclusive licensee American Association for the Advancement of Science. No claim to original U.S. Government Works. Distributed under a Creative Commons Attribution NonCommercial License 4.0 (CC BY-NC).

Polarization photodetectors (pol-PDs) have widespread applications in geological remote sensing, machine vision, biological medicine, and so on. However, commercial pol-PDs use bulky and complicated optical systems with lenses, polarizers, and mechanical spools, which are complex and cumbersome, and respond slowly. Inspired by the desert ants' compound eyes, we developed a single-shot pol-PD based on four-directional grating arrays capped perovskite single-crystal thin film without other standard polarization optics. Our pol-PD has a high detectivity, two orders of magnitude greater than that of commercial photodetectors, and exhibits high polarization sensitivity. The high performance of our pol-PD is due to the highly crystalline perovskite single-crystal thin film and regular nanograting structure, made by a nanoimprinting crystallization method. Our single-shot pol-PD is a compact on-chip optoelectronic device that demonstrates excellent performance in a wide range of applications including accurate bionic navigation, sharp image restoration in hazy scenes, stress visualization of polymers, and detection of cancerous areas in tissues without histological staining.

INTRODUCTION

Polarization photodetectors (pol-PDs) have widespread applications in geological remote sensing, machine vision, biological medicine, and other areas due to their capability for full-parameter vector detection of light waves (*1*, *2*). Commercial pol-PDs, composed of lenses, polarizers, mechanical spools, and photodiodes, are complex and cumbersome, and difficult in miniaturization (*3*, *4*). Recently, to miniaturize pol-PDs, the single-shot on-chip pol-PDs have been developed by using four directional wire grids and metalenses to replace the polarizers and mechanical spools, but there are drawbacks of precise mechanical alignment, optical cross-talk, and light loss (*5*, *6*). In addition, pol-PDs are miniaturized by using intrinsic polarization-sensitive optoelectronic materials including patterned optoelectronic materials (*7*, *8*) and low-dimensional anisotropic materials (*9*, *10*). However, the patterned optoelectronic materials are usually fabricated by photolithography/ion beam etching, which inevitably induces the deterioration of the optoelectrical performance of active layer materials. In addition, the low-dimensional anisotropic materials are difficult to be arranged in program for single-shot imaging (*11*, *12*). Thus, it remains a great challenge to achieve a single-shot on-chip pol-PD with high polarization sensitivity without standard polarization optics.

In nature, the desert ant can travel back to its nest across barren landscapes without any landmarks that simply rely on the polarized skylight perception of its compound eyes (*13*, *14*). One of the Cataglyphis compound eyes consists of ~400 small eyes (Fig. 1, A and B), and each eye has eight photoreceptor cells (*13*). These photoreceptor cells have two sets of microvilli perpendicular to each other (Fig. 1C and fig. S1). The oriented microvilli make these photoreceptor cells sensitive to the polarization direction of the incident light, empowering ants with precise navigation. The unique ability of polarization vision of the desert ant provides the inspiration for fabricating the pol-PD (*15*). Herein, we developed a four-directional grating arrays capped perovskite single-crystal thin film (4D-G-PSCTF) using a one-step solution-crystallization molding method by nanoimprinting (named nanoimprinting crystallization). Four-directional perovskite grating arrays (80 by 80 pixels) are grown and molded directly on the surface of the PSCTF during the crystallization process. The 4D-G-PSCTF has the high crystallization and regular nanograting structure, providing an excellent material for high-performance optoelectronic devices. We constructed an on-chip photodetector based on the 4D-G-PSCTF and achieved highly sensitive single-shot polarization imaging. The detectivity of our pol-PD is two orders of magnitude greater than that of commercial photodetectors. Our pol-PD exhibits high polarization sensitivity without any assistance of other standard polarization optics. Moreover, we demonstrate the wide applications of our single-shot on-chip compact pol-PD in accurate bionic navigation, sharp image restoration in hazy scenes, stress visualization of polymers, and detection of cancerous areas in tissues without histological staining.

RESULTS

Characterization of the eyes of desert ants and the structure of the pol-PD

Figure 1D illustrates the nanoimprinting crystallization method to fabricate the 4D-G-PSCTF. First, we dropped the perovskite solution into a cold substrate (2°C). Second, we covered the solution by a polydimethylsiloxane (PDMS) stamp with 80 by 80 four-directional grating arrays and applied a pressure of 9.8 kPa. The sample was annealed at 100°C for 3 min. Last, the PDMS stamp was peeled off and

[1]CAS Key Laboratory of Bio-inspired Materials and Interface Science, Technical Institute of Physics and Chemistry, Chinese Academy of Sciences, Beijing 100190, P. R. China. [2]School of Transportation Science and Engineering, Beihang University, Beijing 100190, P. R. China. [3]School of Chemistry, Key Laboratory of Bio-inspired Smart Interfacial Science and Technology of Ministry of Education, Beihang University, Beijing 100190, P. R. China. [4]Department of Civil and Environmental Engineering, Imperial College London, London SW7 2AZ, UK. [5]Key Laboratory of Green Printing, Institute of Chemistry, Chinese Academy of Sciences, Beijing 100190, P. R. China. [6]University of Chinese Academy of Sciences, Beijing 100049, P. R. China.
*Corresponding author. Email: mingzhu@mail.ipc.ac.cn
†These authors contributed equally to this work.

Downloaded from https://www.science.org at Imperial College London on December 10, 2024

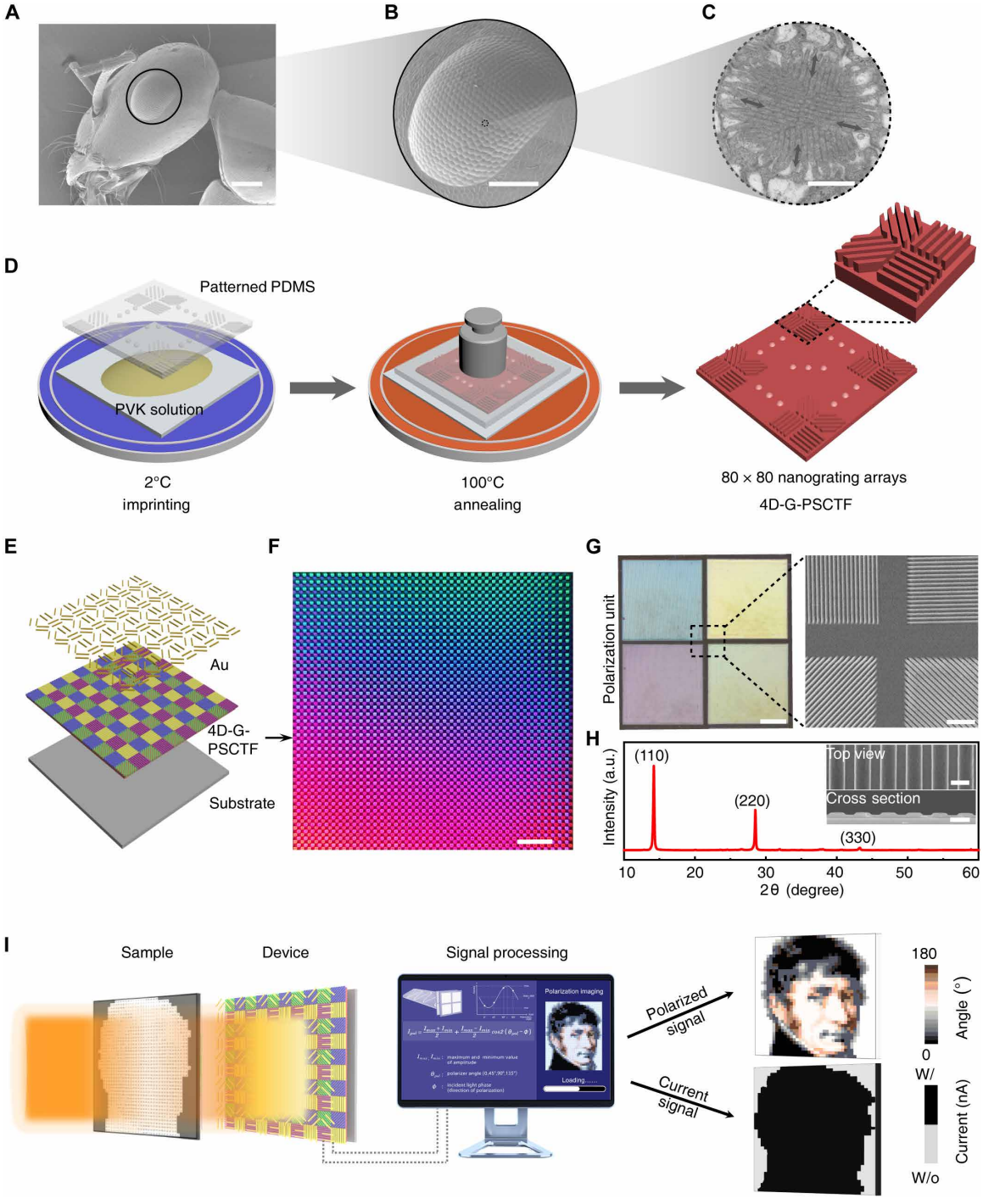


Fig. 1. Desert ant eyes inspired single-shot on-chip pol-PD for polarization imaging. (**A**) SEM image of the head of Cataglyphis. Scale bar, 200 μm. (**B**) SEM image of the Cataglyphis compound eyes. Scale bar, 100 μm. (**C**) TEM image of the cross section of one small eye of the Cataglyphis compound eyes. Scale bar, 0.5 μm. There are two sets of photoreceptor microvilli perpendicular to each other. (**D**) Illustration of the fabrication process of a one-step solution-crystallization molding method by nanoimprinting (named nanoimprinting crystallization) for the 4D-G-PSCTF. PVK solution, perovskite solution. (**E**) Structure of the pol-PD device. The pol-PD is a simple 4D-G-PSCTF with Au electrodes on a glass substrate. (**F**) Optical image of the 4D-G-PSCTF (80 by 80 pixels). Scale bar, 1.5 mm. The samples exhibit vibrant structural colors due to nanograting diffraction. (**G**) Optical microscope image and SEM image of a polarization unit. Scale bar of the optical microscope image, 50 μm. Scale bar of the SEM image, 10 μm. The polarization unit consists of two sets of perpendicular gratings. (**H**) XRD patterns of the G-PSCTF. The insets are the top-view and cross-sectional images of the G-PSCTF. Scale bars, 1 μm. The gratings have a period of 1.5 μm and a height of 150 nm. a.u., arbitrary units. (**I**) Polarization imaging systems. Our polarization imaging system consists of a light source, a sample, and our pol-PD. The 700-nm light that passes through the sample is converted into light with different polarization directions.

Downloaded from https://www.science.org at Imperial College London on December 10, 2024

the 4D-G-PSCTF was obtained. The 4D-G-PSCTF has 80 by 80 multidirectional grating units (grating-0°/45°/90°/135°) (fig. S2). A set of parallel Au electrodes (30 μm in channel width) is deposited on each grating unit to construct a photoconductive device unit (pixel) (fig. S3). Thus, the pol-PD based on the 4D-G-PSCTF consists of 6400 pixels (Fig. 1E). The size of the 4D-G-PSCTF is 12.79 mm by 12.79 mm. The 4D-G-PSCTF shows a vibrant structural color due to grating diffraction (Fig. 1F). Similar to the two sets of perpendicular microvilli in the desert ant eye, four directional grating units (grating-0°⊥ grating-90°, grating-45°⊥, and grating-135°) formed a polarization unit for Stokes polarization detection (Fig. 1G). Figure 1H shows the x-ray diffraction (XRD) pattern of a G-PSCTF (~300 by 300 μm; fig. S4). A set of narrow peaks at (110), (220), and (330) agrees well with the standard pattern of the $CH_3NH_3PbI_3$ ($MAPbI_3$) single crystal (fig. S5) (*16*). The result of a rocking curve (fig. S6) shows that the full width at half maximum for the (110) plane is 0.37°, which is close to that of the bulk $MAPbI_3$ single crystals grown in solution (0.33°) (*16*). In addition, the selected-area electron diffraction (SAED) pattern shows a tetragonal diffraction pattern along the [101] zone axis (fig. S7), which is consistent with the tetragonal structure of $MAPbI_3$ single crystals (*17*). The 4D-G-PSCTF is ~400 nm in thickness and has uniform grating structures with 150 nm in height and 1.5 μm in period (insets in Fig. 1H and fig. S8). All results demonstrate the high crystallization and the uniform grating structures of the 4D-G-PSCTF, which are crucial to the highly sensitive polarization response of the pol-PD. We exploited the prepared pol-PD for polarization imaging. Figure 1I shows a schematic of our polarization imaging system, which consists of a light source, a sample, and our pol-PD. We designed a portrait of É.-L. Malus encoded by polarization patterns in memory of Malus's discovery of the polarization of light (fig. S9). Our pol-PD displays all of the facial features of the portrait, while the planar PD only shows a profile (Fig. 1I). These results demonstrate the polarization sensitivity of our pol-PD and its ability to detect multiple-dimensional information of the objects.

High crystallization mechanism of the 4D-G-PSCTF

We fabricated samples by dropping 5 μl of a perovskite precursor solution onto a cold substrate (2°C) with different drying processes. Three kinds of samples were obtained: a control sample, an unannealed sample, and a 4D-G-PSCTF. The control sample was air dried (fig. S10A). The solutions of the other two samples were first confined by covering a patterned PDMS stamp (fig. S11) under a pressure of 9.8 kPa. One sample was subsequently dried naturally and referred to as the unannealed sample (fig. S10B). The other sample was subsequently annealed in an oven at 100°C for 3 min (fig. S10E), referred to as the 4D-G-PSCTF. As in situ photoluminescence (PL) is often used as an indicator of the performance of perovskite crystallization (*16*), we used the in situ PL spectrometry and optical microscopy (fig. S12) to scrutinize the structural evolution and perovskite crystallization for revealing the mechanism of high crystallization of the 4D-G-PSCTF. Figure 2A shows the snapshots during the growth process of the 4D-G-PSCTF at different times. The in situ PL spectra of the 4D-G-PSCTF and unannealed sample (Fig. 2B and fig. S13) were acquired by an in situ PL measurement system with a temporal resolution of 1 frame/s. A diagram of the perovskite crystallization kinetics was generated based on the in situ PL spectra and optical microscopy imaging results (Fig. 2C).

We designate three crystallization stages during the crystallization process: stage I, natural evaporation of the solution induced nucleation; stage II, space-confined annealing regulated ripening; and stage III, space-confined crystal growth over a large area. In the first stage, the solvent spread on the substrate and evaporated rapidly in the air, quickly surpassing C_{min} and bursting many nuclei. In Fig. 2B and fig. S13B, there were no PL signals during the process in the first 25 s because there were few initial nuclei. When the process proceeded for 25 s, the PL signals of the unannealed sample (fig. S13B, I, 0 to 101 s) and the 4D-G-PSCTF (Fig. 2B, I, 0 to 61 s) both appeared and then gradually increased, indicating the continuous production of the perovskite nucleus (*18*). In the second stage, the solution was confined between the PDMS stamp and the substrate. The solvent evaporation rate decreased. For the unannealed sample, the temperature of the solution increased from 2°C to room temperature (the blue curve in Fig. 2C). For the 4D-G-PSCTF, the temperature of the solution increased from 2°C to 100°C (the red curve in Fig. 2C). The relative PL intensities of the unannealed sample (fig. S13B, II, 101 to 166 s) and 4D-G-PSCTF (Fig. 2B, II, 61 to 145 s) both decreased, indicating the reduction of perovskite nuclei and the growth of large perovskite grains caused by the Oswald ripening. Moreover, in situ microscopy revealed the gradual generation and enhancement of structural color during the second stage (Fig. 2A and fig. S13A). The 4D-G-PSCTF showed a brighter structural color than the unannealed sample, which demonstrated that the grating structure of the 4D-G-PSCTF was better than that of the unannealed sample. In the second stage, the solution concentration of the unannealed sample remained between C_s and C_{min} at 25°C. For the 4D-G-PSCTF, the solution concentration remained between C'_s and C'_{min} at 100°C. The homogeneous nucleation in the crystallization process of the unannealed sample and 4D-G-PSCTF was inhibited. The ripening process lead to a decrease in perovskite nucleation and an increase in solute, which favored the growth of large grains. For the crystallization process of the 4D-G-PSCTF, the annealing step promoted early ripening. The ripening process of the 4D-G-PSCTF started at 61 s (Fig. 2B, II), while that of the unannealed sample started at 101 s (fig. S13B, II). Moreover, the ripening time of the 4D-G-PSCTF ($\Delta t = 84$ s) was increased by 19 s compared with that of the unannealed sample ($\Delta t_1 = 65$ s), resulting in sufficient ripening. Therefore, the annealing process provided sufficient ripening and facilitated the complete dissolution of small grains and the formation of large perovskite crystals. In the third stage, the PL intensities of the unannealed (fig. S13B, III, 166 to 300 s) and 4D-G-PSCTF (Fig. 2B, III, 145 to 300 s) gradually increased, and their PL peak positions were both red shifted, indicating the growth of perovskite grains (Fig. 2B and fig. S13B) (*16*). The PL intensity of the 4D-G-PSCTF (Fig. 2B) was stronger than that of the unannealed sample (fig. S13B). Moreover, the 4D-G-PSCTF showed bright structural colors (Fig. 2A) as its grating structure was uniform and regular (inset in Fig. 2C). On the other hand, the unannealed sample showed weak structural colors (fig. S13A) due to the presence of many defects and an irregular structure (inset in Fig. 2C). We obtained a grain boundary-free 4D-G-PSCTF via our nanoimprinting crystallization method. Space-confined growth and the annealing process can well control the nucleation and growth of perovskite, facilitating the formation of high-quality perovskite.

The performance of pol-PD based on a G-PSCTF

Researchers usually use the planar perovskite films to prepare photodetectors (*19*, *20*). However, there is notable light loss due to Fresnel reflection. Our group first constructed a grating structure on the

Downloaded from https://www.science.org at Imperial College London on December 10, 2024

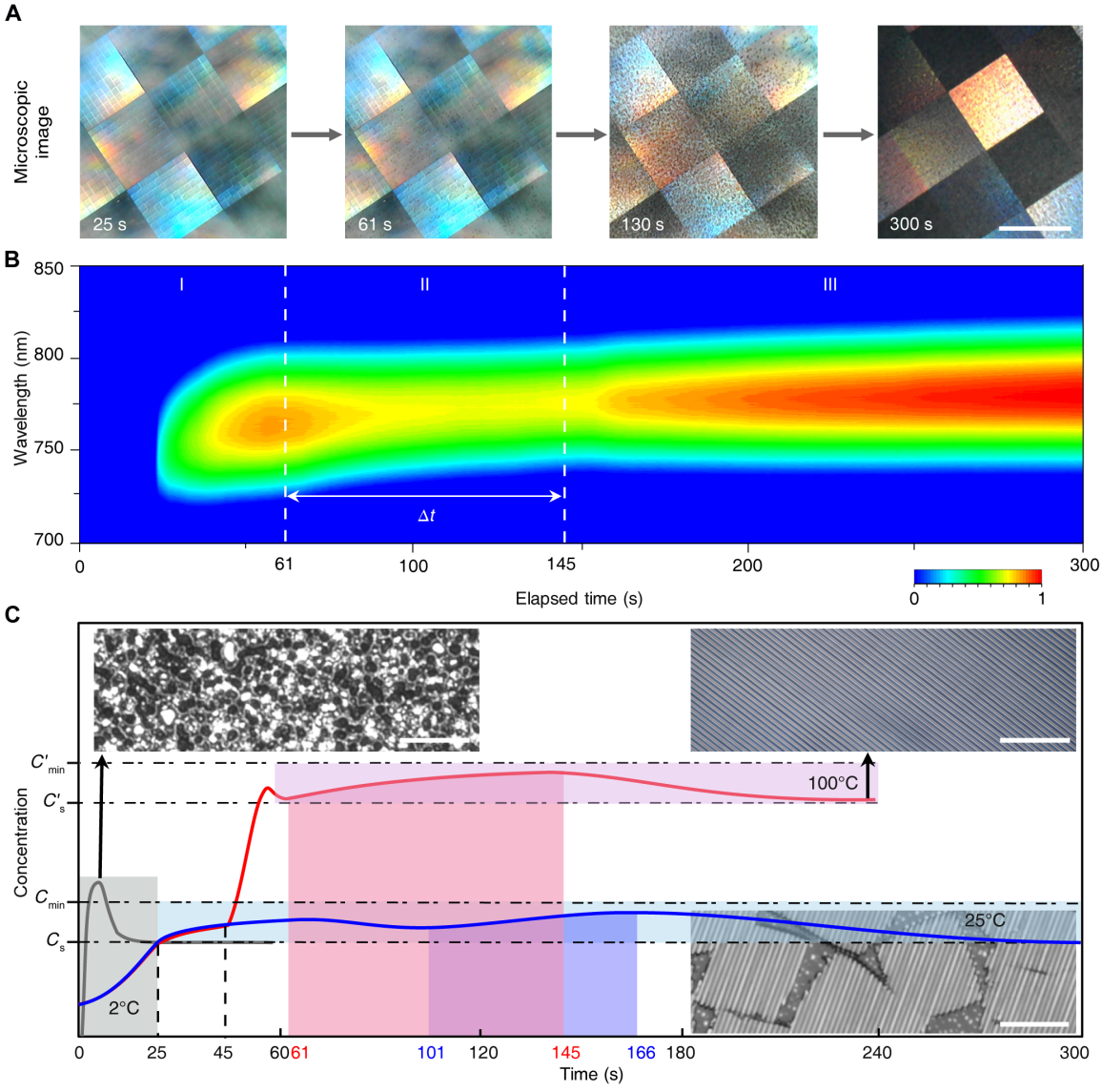


Fig. 2. High crystallization mechanism of the 4D-G-PSCTF. (**A**) Snapshots during the growth process of the 4D-G-PSCTF at different times. Scale bar, 2 mm. To observe the structural color change of the 4D-G-PSCTF more clearly, we enlarged the single pixel area to 2 mm by 2 mm. (**B**) In situ PL spectrum of the 4D-G-PSCTF. $\Delta t = 84$ s is the ripening time of perovskite. (**C**) Diagram of the crystallization kinetics of three kinds of samples. C_s and C'_s are defined as the minimum critical concentration for heterogeneous nucleation at 25° and 100°C, respectively. C_{min} and C'_{min} are defined as the minimum critical concentration for homogeneous nucleation at 25° and 100°C, respectively. Scale bars, 20 μm.

surface of perovskite films to improve the light harvesting capability of the photodetectors and endow the polarization sensitivity of the photodetectors (*21*–*24*). In this work, we integrated four-directional grating arrays with a PSCTF and obtained a 4D-G-PSCTF. Figure 3 (A to C) and fig. S14 show the antireflectivity, absorption, light harvesting efficiency (LHE) (*21*), carrier lifetime, and carrier mobility of a grating unit (G-PSCTF), which are increased greatly compared with those of the planar PSCTF. Compared with that of the planar PSCTF, the reflectivity of the G-PSCTF is decreased by 4.6% and its absorption is increased by 4% at wavelengths ranging from 400 to 800 nm (Fig. 3A). The grating structures can reduce the reflection and prolong the optical path length in the active layer of the G-PSCTF through multiple scattering (Fig. 3D) (*25*), leading to a 6% increase in the LHE (Fig. 3A). In addition, we simulated the time-averaged electromagnetic energy density with respect to the *x*-*z* plane at 700-nm wavelength and the absorption at wavelengths ranging from 400 to 800 nm of the G-PSCTF and planar PSCTF (Fig. 3E and fig. S15, A and B). Clearly, more light energy is confined in the G-PSCTF (Fig. 3E), leading to highly efficient interactions between the light and the perovskite. In contrast, the light energy in the planar PSCTF is concentrated at the interface between the air and the perovskite, resulting in large energy losses. The PL intensity (fig. S16) and carrier lifetime (Fig. 3B) of the G-PSCTF are two and four times greater than those of planar PSCTF, respectively. The enhanced PL intensity and the increased carrier lifetime indicated a decrease in nonradiative recombination in the G-PSCTF. The carrier mobility of the G-PSCTF ($41.56\ cm^2\ V^{-1}\ s^{-1}$) is 22% greater than that of the planar PSCTF ($32.72\ cm^2\ V^{-1}\ s^{-1}$) (Fig. 3C). Compared with that of the planar PSCTF,

Downloaded from https://www.science.org at Imperial College London on December 10, 2024

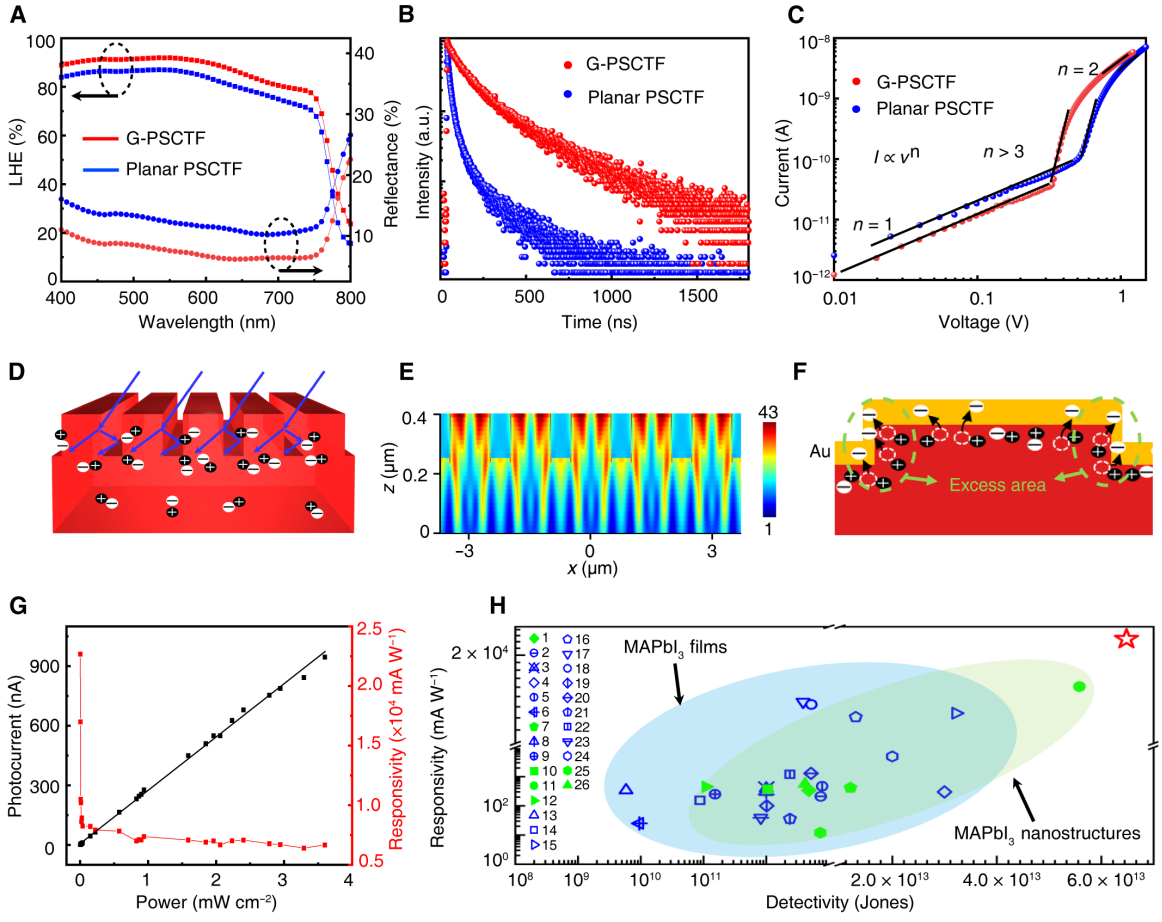


Fig. 3. Performance of the pol-PD based on a G-PSCTF. (**A**) LHE and reflectance of the G-PSCTF and planar PSCTF. The G-PSCTF shows higher LHE and lower reflectance than the planar PSCTF at wavelength of 400 to 800 nm. (**B**) TRPL curves of the G-PSCTF and planar PSCTF. The carrier lifetime of the G-PSCTF (τ_1 = 85.24 ns) is four times higher than that of the planar PSCTF (τ_1 = 21.82 ns). (**C**) *I-V* curve showing three different regions for the G-PSCTF and planar PSCTF. The regions are marked for ohmic ($I \propto V^{n=1}$), TFL (trap-filled limited) ($I \propto V^{n=3}$), and Child's regime ($I \propto V^{n=2}$). The carrier mobility of the G-PSCTF (41.56 $cm^2 V^{-1} s^{-1}$) is higher than that of the planar PSCTF (32.72 $cm^2 V^{-1} s^{-1}$). (**D**) Grating structure enhances light trapping facilitating more carrier generation. (**E**) Field plots of time-averaged electromagnetic energy density with respect to the *x-z* plane at the light wavelength of 700 nm for the G-PSCTF. The G-PSCTF exhibits excellent light harvesting ability. (**F**) Schematic of carrier collection for the pol-PD. (**G**) Photocurrent and responsivity at the powers of 700-nm incident light ranging from 2.2 μW cm^{-2} to 3.59 mW cm^{-2}. (**H**) Responsivity and detectivity of the pol-PD compared with other works.

the contact area between the G-PSCTF and Au increased by 20%, facilitating more efficient carrier transport and extraction in the device (Fig. 3F and fig. S15, C and D). In summary, our pol-PD exhibited a large improvement in light trapping capability and carrier extraction efficiency, which contributed to its high performance.

We tested the optoelectronic performance of the pol-PD. Under illumination (3-V bias, 700 nm, and 3.59 mW cm^{-2}), the photocurrent (fig. S17) and on/off ratio (fig. S18) of the pol-PD are 3 times and 10 times greater than those of the planar PD, respectively. The dark current of the pol-PD (15 pA) is three times smaller than that of the planar PD (48 pA; fig. S19). Moreover, the pol-PD exhibited a fast response time of 1.67 ms and recovery time of 1.89 ms (fig. S20). These results demonstrate that the pol-PD has greater light sensitivity than the planar PD and has a fast response. Furthermore, we tested the dependence of the photocurrent and responsivity on the illumination intensities ranging from 2.2 μW cm^{-2} to 3.59 mW cm^{-2}. The pol-PD has a linear dynamic range (LDR) value of 84 dB, which is larger than that of the planar PD (60 dB) and commercial InGaAs PD (66 dB) (*26*). The large LDR indicates that the pol-PD can be used over a wide range of light powers. Under illumination (3-V bias, 700 nm, and 2.2 μW cm^{-2}), the responsivity of the pol-PD (22,680 mA W^{-1}) is approximately twice higher than that of the planar PD (11,640 mA W^{-1}) (Fig. 3G and fig. S21). The detectivity based on the dark current of our pol-PD (6.5×10^{13} Jones) is 3.6 times greater than that of the planar PD (1.8×10^{13} Jones) and 10 to 100 times greater than that of commercial InGaAs or silicon PD (10^{11} to 10^{12} Jones) (fig. S22). Besides, if the detectivity is calculated based on photoresponse and noise current results, the detectivity of our pol-PD is 4.5 times greater than that of the planar PD (fig. S23). Compared with the reported $MAPbI_3$-based PDs, the key parameters of the device are summarized in Fig. 3H (table S1). The responsivity and detectivity of our pol-PD exceeds those of all previously reported $MAPbI_3$-based PDs. Moreover, our pol-PD exhibited good cycling stability and long-term stability. At a light intensity of 1.71 mW cm^{-2}, the pol-PD showed smooth light on/off cycles at 1 to 5 V (fig. S24). The unencapsulated devices were stored at 25°C with

Downloaded from https://www.science.org at Imperial College London on December 10, 2024

~30% humidity, and the photocurrent was tested every 10 days. As shown in fig. S25, after 2160 hours of storage, the photocurrent of the pol-PD remained at 90% of its initial value, while the performance of the planar PD drops to 70% of its initial value (fig. S26).

Application of bionic navigation and polarization imaging

Inspired by the compound eyes of desert ants, we constructed a single-shot on-chip pol-PD with a 4D-G-PSCTF for bionic navigation and polarization imaging (Fig. 4A). A 4D-G-PSCTF with four different grating directions (0°, 90°, 45°, and 135°) formed a polarization unit. The pol-PD exhibited an excellent polarization ratio of 1.73 at the wavelength of 700 nm (Fig. 4B and fig. S27), which facilitated successful bionic navigation and polarization imaging. The polarization ratio of the device reached a maximum value of 2.22 at 750 nm (fig. S28). We integrated the pol-PD (6 by 6 pixels) with the open-source electronic platform of Arduino UNO for digital testing (figs. S29 to S31). When polarized light is irradiated onto the pol-PD, each polarization unit of the pol-PD feeds back four current

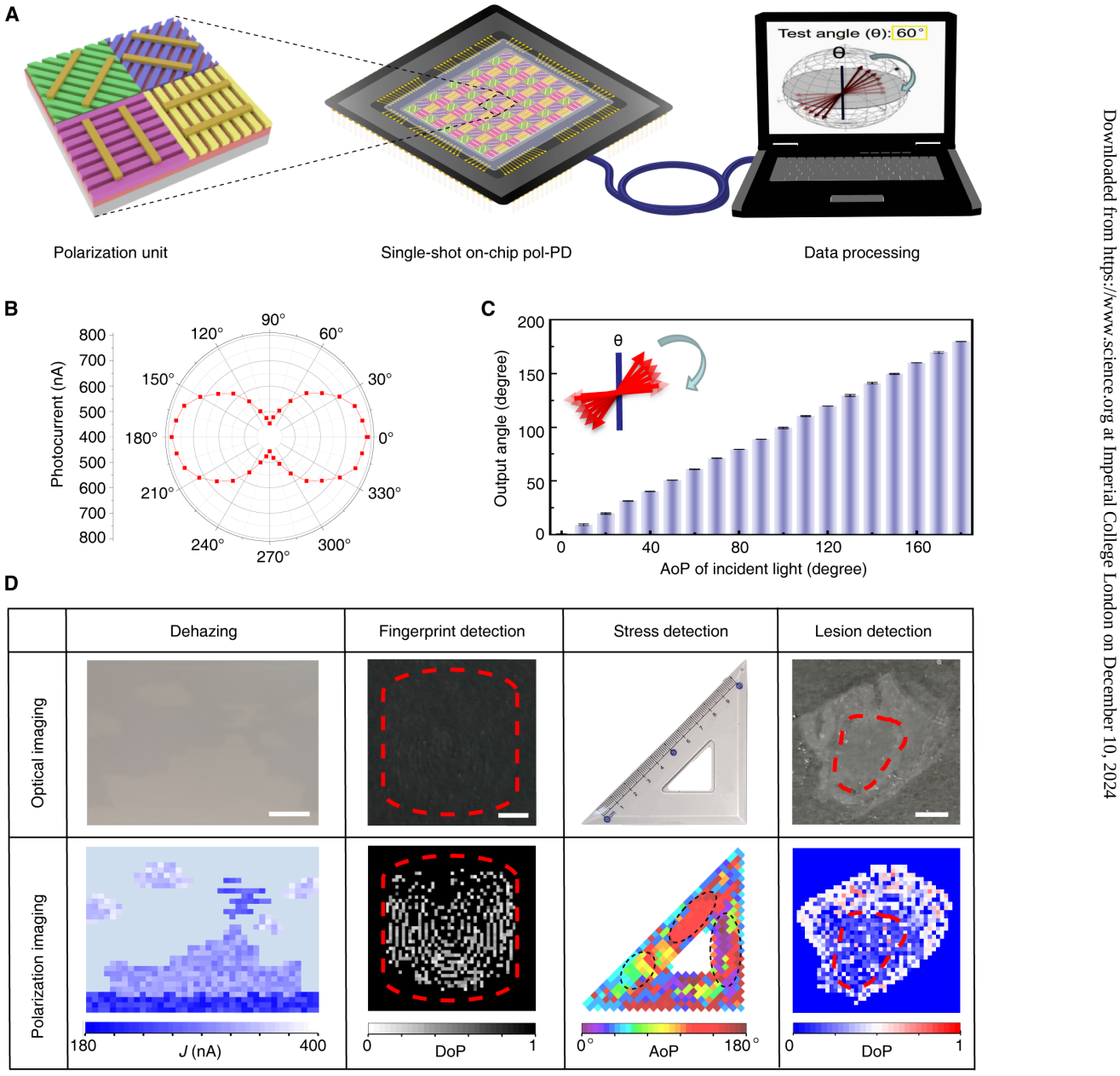


Fig. 4. Application of bionic navigation and polarization imaging. (**A**) Working mechanism diagram of our single-shot on-chip pol-PD. (**B**) Photocurrent dependence of the pol-PD on AoP of incident light (0° to 360°). The pol-PD has a high polarization sensitivity (I_{max}/I_{min} = 1.73). (**C**) Relationship between the AoP of device output and the AoP of incident light. The error between the AoP of incident light and the output angle is ±1.2. (**D**) Applications of polarization imaging. We exploited our pol-PD to realize dehazing imaging (scale bar, 1 cm), fingerprint detection (scale bar, 2 mm), stress detection of the ruler, and the detection of the cancerous area in rectal tissue (scale bar, 2 mm).

Downloaded from https://www.science.org at Imperial College London on December 10, 2024

values, I_0, I_{90}, I_{45}, and I_{135}. The angle of polarization (AoP) and degree of polarization (DoP) of the polarized light are calculated based on the algorithm of the Stokes vector (Supplementary Text). The test accuracy of the AoP and DoP is only ±1.2° and ±0.1, respectively (Fig. 4C and fig. S32). These results show that our pol-PD enables accurate bionic polarization navigation.

We constructed a high-performance 80 by 80 pixels pol-PD (fig. S33) and exploited it for polarization imaging. We simulated the time-averaged electromagnetic energy density with respect to the *x*-*y* plane and the *x*-*z* plane at a wavelength of 700 nm for a polarization unit (fig. S34). There is no optical cross-talk between the four pixels. In addition, we randomly tested the electrical stability and the correlation between the photocurrent and AoP of 80 pixel units. Each pixel unit showed a stable current intensity with the incident light intensities ranging from 1.02 to 3.59 mW cm^{-2} (fig. S35). The current values of each pixel unit are sinusoidal to the AoP of incident light ranging from 0° to 720°, indicating the good polarization responsivity of the pol-PD (fig. S36). Each polarization unit has four photocurrents, which are denoted as I_0, I_{90}, I_{45}, and I_{135}. The DoP and AoP are reconstructed based on the Stokes vector (Supplementary Text and fig. S37). Polarization imaging can enhance the contrast between objects, capture detailed features, and dehaze and is widely applied in the fields of machine vision and biomedicine (*27*, *28*). To demonstrate the polarization dehazing ability of our pol-PD, we constructed a polarization imaging system that included polarized light, a sample, a simulated haze scene, and the pol-PD (fig. S38). The sample was made of yellow transparent laminating tapes, and the layer numbers of the laminating tapes vary in different zones (fig. S39). Figure 4D shows an optical image and a polarization image of the sample under haze conditions. Our pol-PD achieved sharp image restoration in hazy scenes via a dehazing algorithm (Supplementary Text) because the polarization information of multilayer tapes varied according to the layer number. In contrast, the optical image of the sample became invisible under haze conditions. In addition, we used the pol-PD to detect fingerprint impressions and the stress distribution in the plastic ruler compared with the common camera. The polarization image of the fingerprint impression obtained by our pol-PD is sharp and has many details, while no fingerprint image was obtained by the camera. Similarly, the stress distribution in the plastic ruler was observed by the pol-PD due to the birefringence effect of the plastic ruler, while only a topographic image of the ruler was observed by the camera (Fig. 4D). Furthermore, the pol-PD can directly display the cancerous area of rectal tissue under polarized light without histological staining (Fig. 4D).

DISCUSSION

We developed a simple nanoimprinting crystallization method for preparing highly crystalline 4D-G-PSCTF and constructed a single-shot high-performance pol-PD (80 by 80 pixels) without standard polarization optics. We optimized our fabrication method and well controlled the nucleation and the ripening time to ensure the high crystallinity of the 4D-G-PSCTF. Our pol-PD exhibited a record-high responsivity (22,680 mA W^{-1}) and detectivity (6.5×10^{13} Jones) among all reported $MAPbI_3$-based PDs. In addition, the uniform grating structure endows the device with a polarization sensitivity of I_{max}/I_{min} as high as 1.73. The high performance of our pol-PD endows it with great potential for polarization imaging. We have achieved success in bionic navigation, visual dehazing, sharp fingerprint imaging, stress visualization of polymers, and detection of cancerous areas in tissues without histological staining. Thus, our pol-PD provides a simple cost-effective polarization imaging system with high sensitivity and enables the widespread adoption of polarization imaging.

MATERIALS AND METHODS

Materials

Methylammonium iodide (MAI; 99%), lead iodide (PbI_2; 99.999%), acetonitrile (ACN; 99.9%), and methylamine ethanol solution (33 wt %) were purchased from Sigma-Aldrich. A four-directional array template was customized at Suzhou Impression Technology Co. Ltd. Au particles were purchased from Zhong Nuo Advanced Material Technology Co. Ltd. Frozen sections of rectal tissue with cancerous areas were obtained from the Second Affiliated Hospital of Soochow University. All experiments were performed in compliance with relevant Chinese and institutional laws and guidelines. Informed consent was obtained from all patients.

Preparation of precursor solutions

A solution of methylamine ethanol solution (33 wt %) was placed into a Dreschel bottle, which was kept in an ice bath. Nitrogen (N_2) was then bubbled into the solution, thus degassing the solution of MA. The produced MA gas was passed through a polyvinylidene fluoride membrane filter head (0.22 μm) into the perovskite solution at a concentration of 1 M, which consisted of an ACN solution and a perovskite precursor (1 M MAI:1 M PbI_2). The gas was bubbled into the perovskite solution until the perovskite particles were completely dissolved, resulting in a clear, light yellow solution. After all particulates in the solution were dissolved, the vial containing the solution was sealed and stored at 2°C until needed. The solution was removed from the stock as needed, after which the vial was resealed and returned to the refrigerator.

Fabrication of the PDMS stamp with grating arrays

The PDMS monomer and the cross-linking agent (mass ratio, 10:1) were evenly stirred, and the bubbles were removed by centrifugation. A template with four-directional grating arrays was placed in a petri dish. The configured PDMS solution was poured into the petri dish and then placed under vacuum at a negative pressure of 5 Pa for 30 min to remove air bubbles. Next, the petri dish was heated on a hot plate at 70°C for 2 hours to obtain a PDMS stamp with grating arrays.

Preparation of the 4D-G-PSCTF

The glass substrates were ultrasonically cleaned with deionized water, ethanol, acetone, and isopropanol and subsequently treated with plasma at 200 W for 300 s. First, the treated glass substrates were placed on a cold platform at 2°C. Then, the perovskite precursor solution (5 μl) was added dropwise to the glass substrates. A prepatterned PDMS stamp was capped on top of the solution, and a pressure of 9.8 kPa was applied. Last, the samples were annealed in an oven at 100°C for 3 min.

Characterization

SEM, TEM, and AFM images were obtained by scanning electron microscopy (SEM; JSM-7500F, JEOL, Japan), transmission electron microscopy (TEM; FEI Tecnai G2 F30, United States), and atomic force

Downloaded from https://www.science.org at Imperial College London on December 10, 2024

microscopy (AFM; Bruker, Germany), respectively. Polarized optical images of perovskite films were obtained by polarization microscopy (Nikon, ECLIPSE LV100N POL). XRD and grazing incidence wide-angle x-ray scattering patterns were measured by an x-ray diffractometer (D/max 2500, Rigaku, Japan) and wide-angle x-ray scattering system (Xeuss 2.0, France). The rocking curves were measured using a PANalytical Empyrean x-ray powder diffractometer. Absorption and transmission spectra were collected with a ultraviolet-visible spectrophotometer (Shimadzu, UV-2600). Steady-state PL and time-resolved PL (TRPL) were characterized by a steady state transient fluorescence spectrometer (FLS980, Edinburgh, United Kingdom). The crystallization process of the perovskite was monitored by a custom in situ PL measurement system. The optoelectronic performances were determined by a micromanipulation probe station (Keithley 4200, Keithley, United States). The light was generated from a wide-band laser source (NKT Photonics). Light intensity was measured by an optical power meter (PM100D, Thorlabs). The photoresponse time was measured by a KEYSIGHT oscilloscope (B2912a, China). Long-term stability was recorded by storing the unencapsulated device in a box at 30% relative humidity and 25°C.

Optical simulations

The finite-difference time-domain method was used to numerically calculate the time-averaged electromagnetic energy density in the perovskite layer. A full three-dimensional model of one unit cell with periodic boundary conditions and a plane wave excitation normal to the perovskite was used. The complex valued refractive indices between the wavelengths of 400 to 800 nm for the perovskite material were obtained by ellipsometry, and the refractive indices of the glass substrate were assumed to be constant with $n_{(\mathrm{glass})} = 1.5$.

Supplementary Materials

The PDF file includes:

Supplementary Text
Figs. S1 to S40
Table S1
Legend for data S1
References

Other Supplementary Material for this manuscript includes the following:

Data S1

REFERENCES AND NOTES

1. M. Dai, C. Wang, B. Qiang, F. Wang, M. Ye, S. Han, Y. Luo, Q. J. Wang, On-chip mid-infrared photothermoelectric detectors for full-Stokes detection. *Nat. Commun.* **13**, 4560 (2022).
2. N. A. Rubin, G. D'Aversa, P. Chevalier, Z. Shi, W. T. Chen, F. Capasso, Matrix Fourier optics enables a compact full-Stokes polarization camera. *Science* **365**, eaax1839 (2019).
3. J. Wei, Y. Chen, Y. Li, W. Li, J. Xie, J. Xie, C. Lee, K. S. Novoselov, C.-W. Qiu, Geometric filterless photodetectors for mid-infrared spin light. *Nat. Photonics* **17**, 171–178 (2023).
4. J. Wei, C. Xu, B. Dong, C.-W. Qiu, C. Lee, Mid-infrared semimetal polarization detectors with configurable polarity transition. *Nat. Photonics* **15**, 614–621 (2021).
5. A. Arbabi, A. Faraon, Advances in optical metalenses. *Nat. Photonics* **17**, 16–25 (2023).
6. A. Arbabi, Y. Horie, M. Bagheri, A. Faraon, Dielectric metasurfaces for complete control of phase and polarization with subwavelength spatial resolution and high transmission. *Nat. Nanotechnol.* **10**, 937–943 (2015).
7. C. Huang, C. Zhang, S. Xiao, Y. Wang, Y. Fan, Y. Liu, N. Zhang, G. Qu, H. Ji, J. Han, L. Ge, Y. Kivshar, Q. Song, Ultrafast control of vortex microlasers. *Science* **367**, 1018–1021 (2020).
8. Y. Chen, J. Feng, Y. Huang, W. Chen, R. Su, S. Ghosh, Y. Hou, Q. Xiong, C.-W. Qiu, Compact spin-valley-locked perovskite emission. *Nat. Mater.* **22**, 1065–1070 (2023).
9. L. Tong, X. Huang, P. Wang, L. Ye, M. Peng, L. An, Q. Sun, Y. Zhang, G. Yang, Z. Li, F. Zhong, F. Wang, Y. Wang, M. Motlag, W. Wu, G. J. Cheng, W. Hu, Stable mid-infrared polarization imaging based on quasi-2D tellurium at room temperature. *Nat. Commun.* **11**, 2308 (2020).
10. H. Yuan, X. Liu, F. Afshinmanesh, W. Li, G. Xu, J. Sun, B. Lian, A. G. Curto, G. Ye, Y. Hikita, Z. Shen, S.-C. Zhang, X. Chen, M. Brongersma, H. Y. Hwang, Y. Cui, Polarization-sensitive broadband photodetector using a black phosphorus vertical p–n junction. *Nat. Nanotechnol.* **10**, 707–713 (2015).
11. Y. Gao, J. Liao, H. Chen, H. Ning, Q. Wu, Z. Li, Z. Wang, X. Zhang, M. Shao, Y. Yu, High performance polarization-resolved photodetectors based on intrinsically stretchable organic semiconductors. *Adv. Sci.* **10**, 2204727 (2022).
12. L. Gu, S. Poddar, Y. Lin, Z. Long, D. Zhang, Q. Zhang, L. Shu, X. Qiu, M. Kam, A. Javey, Z. Fan, A biomimetic eye with a hemispherical perovskite nanowire arrays retina. *Nature* **581**, 278–282 (2020).
13. M. Collett, T. S. Collett, S. Bisch, R. Wehner, Local and global vectors in desert ant navigation. *Nature* **394**, 269–272 (1998).
14. W. Zhang, Y. Cao, X. Zhang, Z. Liu, Sky light polarization detection with linear polarizer triplet in light field camera inspired by insect vision. *Appl. Opt.* **54**, 8962–8970 (2015).
15. J. Pan, Y. Wu, X. Zhang, J. Chen, J. Wang, S. Cheng, X. Wu, X. Zhang, J. Jie, Anisotropic charge trapping in phototransistors unlocks ultrasensitive polarimetry for bionic navigation. *Nat. Commun.* **13**, 6629 (2022).
16. Y. Yamada, T. Yamada, L. Q. Phuong, N. Maruyama, H. Nishimura, A. Wakamiya, Y. Murata, Y. Kanemitsu, Dynamic optical properties of $CH_3NH_3PbI_3$ single crystals as revealed by one- and two-photon excited photoluminescence measurements. *J. Am. Chem. Soc.* **137**, 10456–10459 (2015).
17. G. Wang, D. Li, H.-C. Cheng, Y. Li, C.-Y. Chen, A. Yin, Z. Zhao, Z. Lin, H. Wu, Q. He, M. Ding, Y. Liu, Y. Huang, X. Duan, Wafer-scale growth of large arrays of perovskite microplate crystals for functional electronics and optoelectronics. *Sci. Adv.* **1**, e1500613 (2015).
18. S. Pratap, F. Babbe, N. S. Barchi, Z. Yuan, T. Luong, Z. Haber, T.-B. Song, J. L. Slack, C. V. Stan, N. Tamura, C. M. Sutter-Fella, P. Muller-Buschbaum, Out-of-equilibrium processes in crystallization of organic-inorganic perovskites during spin coating. *Nat. Commun.* **12**, 5624 (2021).
19. B.-S. Qiao, S.-Y. Wang, Z.-H. Zhang, Z.-D. Lian, Z.-Y. Zheng, Z.-P. Wei, L. Li, K. W. Ng, S.-P. Wang, Z.-B. Liu, Photosensitive dielectric 2D perovskite based photodetector for dual wavelength demultiplexing. *Adv. Mater.* **35**, e2300632 (2023).
20. Z. Li, Z. Chen, Z. Shi, G. Zou, L. Chu, X.-K. Chen, C. Zhang, S. K. So, H.-L. Yip, Charge injection engineering at organic/inorganic heterointerfaces for high-efficiency and fast-response perovskite light-emitting diodes. *Nat. Commun.* **14**, 6441 (2023).
21. Y. Wang, P. Wang, X. Zhou, C. Li, H. Li, X. Hu, F. Li, X. Liu, M. Li, Y. Song, Diffraction-grated perovskite induced highly efficient solar cells through nanophotonic light trapping. *Adv. Energy. Mater.* **8**, 1702960 (2018).
22. Y. Zhan, Y. Wang, Q. Cheng, C. Li, K. Li, H. Li, J. Peng, B. Lu, Y. Wang, Y. Song, L. Jiang, M. Li, A butterfly-inspired hierarchical light-trapping structure towards a high-performance polarization-sensitive perovskite photodetector. *Angew. Chem. Int. Ed. Engl.* **58**, 16456–16462 (2019).
23. Y. Wang, Y. Lan, Q. Song, F. Vogelbacher, T. Xu, Y. Zhan, M. Li, W. E. I. Sha, Y. Song, Colorful efficient moire-perovskite solar cells. *Adv. Mater.* **33**, 2008091 (2021).
24. Q. Song, Y. Wang, F. Vogelbacher, Y. Zhan, D. Zhu, Y. Lan, W. Fang, Z. Zhang, L. Jiang, Y. Song, M. Li, Moiré perovskite photodetector toward high-sensitive digital polarization imaging. *Adv. Energy Mater.* **11**, 2100742 (2021).
25. E. R. Martins, J. Li, Y. Liu, J. Zhou, T. F. Krauss, Engineering gratings for light trapping in photovoltaics: The supercell concept. *Phys. Rev. B* **86**, 041404 (2012).
26. L. Dou, Y. Yang, J. You, Z. Hong, W.-H. Chang, G. Li, Y. Yang, Solution-processed hybrid perovskite photodetectors with high detectivity. *Nat. Commun.* **5**, 5404 (2014).
27. J. Li, Y.-C. Hung, O. Kulce, D. Mengu, A. Ozcan, Polarization multiplexed diffractive computing: All-optical implementation of a group of linear transformations through a polarization-encoded diffractive network. *Light Sci. Appl.* **11**, 153 (2022).
28. W. Ran, Z. Ren, P. Wang, Y. Yan, K. Zhao, L. Li, Z. Li, L. Wang, J. Yang, Z. Wei, Z. Lou, G. Shen, Integrated polarization-sensitive amplification system for digital information transmission. *Nat. Commun.* **12**, 6476 (2021).
29. M. Born, E. Wolf, E. Hecht, Principles of optics: Electromagnetic theory of propagation, interference and diffraction of light. *Phys. Today* **53**, 77–78 (2000).
30. H. Israël, F. Kasten, "[KOSCHMIEDERs Theorie der horizontalen Sichtweite]" in *Die Sichtweite im Nebel und die Möglichkeiten ihrer künstlichen Beeinflussung* (Springer, 1959), pp. 7–10.
31. Y. Y. Schechner, S. G. Narasimhan, S. K. Nayar, Polarization-based vision through haze. *Appl. Opt.* **42**, 511–525 (2003).
32. C. Liu, K. Wang, C. Yi, X. Shi, P. Du, A. W. Smith, A. Karim, X. Gong, Ultrasensitive solution-processed perovskite hybrid photodetectors. *J. Mater. Chem. C* **3**, 6600–6606 (2015).
33. Y. Fang, J. Huang, Resolving weak light of sub-picowatt per square centimeter by hybrid perovskite photodetectors enabled by noise reduction. *Adv. Mater.* **27**, 2804–2810 (2015).
34. B. R. Sutherland, A. K. Johnston, A. H. Ip, J. Xu, V. Adinolfi, P. Kanjanaboos, E. H. Sargent, Sensitive, fast, and stable perovskite photodetectors exploiting interface engineering. *ACS Photonics* **2**, 1117–1123 (2015).

Downloaded from https://www.science.org at Imperial College London on December 10, 2024

35. Y. Wang, D. Yang, X. Zhou, D. Ma, A. Vadim, T. Ahamad, S. M. Alshehri, Perovskite/polymer hybrid thin films for high external quantum efficiency photodetectors with wide spectral response from visible to near-infrared wavelengths. *Adv. Opt. Mater.* **5**, 1700213 (2017).
36. L. Shen, Y. Fang, D. Wang, Y. Bai, Y. Deng, M. Wang, Y. Lu, J. Huang, A self-powered, sub-nanosecond-response solution-processed hybrid perovskite photodetector for time-resolved photoluminescence-lifetime detection. *Adv. Mater.* **28**, 10794–10800 (2016).
37. S. Du, G. Li, X. Cao, Y. Wang, H. Lu, S. Zhang, C. Liu, H. Zhou, Oxide semiconductor phototransistor with organolead trihalide perovskite light absorber. *Adv. Electron. Mater.* **3**, 1600325 (2017).
38. S.-F. Leung, K.-T. Ho, P.-K. Kung, V. K. S. Hsiao, H. N. Alshareef, Z. L. Wang, J.-H. He, A self-powered and flexible organometallic halide perovskite photodetector with very high detectivity. *Adv. Mater.* **30**, 1704611 (2018).
39. Y. Zhang, Z. Qin, W. Nie, Y. Li, X. Huo, D. Song, B. Qiao, Z. Xu, S. Wageh, A. Al-Ghamdi, S. Zhao, High-performance $MAPbI_3/PM_6$:Y_6 perovskite/organic hybrid photodetectors with a broadband response. *Adv. Opt. Mater.* **10**, 2200648 (2022).
40. J. Ghosh, G. Natu, P. K. Giri, Plasmonic hole-transport-layer enabled self-powered hybrid perovskite photodetector using a modified perovskite deposition method in ambient air. *Org. Electron.* **71**, 175–184 (2019).
41. Z. Liu, X. Liu, B. Sun, X. Tan, H. Ye, J. Zhou, Z. Tang, T. Shi, G. Liao, A Cu-doping strategy to enhance photoelectric performance of self-powered hole-conductor-free perovskite photodetector for optical communication applications. *Adv. Mater. Technol.* **5**, 2000260 (2020).
42. M. Wang, F. Cao, L. Meng, W. Tian, L. Li, High-performance flexible self-powered photodetector based on perovskite and low-temperature processed In_2S_3 nanoflake film. *Adv. Mater. Interfaces* **6**, 1801526 (2019).
43. J. M. Kim, S. Kim, S.-H. Choi, High-performance *n-i-p*-type perovskite photodetectors employing graphene-transparent conductive electrodes N-type doped with amine group molecules. *ACS Sustain. Chem. Eng.* **7**, 734–739 (2019).
44. S. Chen, C. Teng, M. Zhang, Y. Li, D. Xie, G. Shi, A flexible UV–Vis–NIR photodetector based on a perovskite/conjugated-polymer composite. *Adv. Mater.* **28**, 5969–5974 (2016).
45. Y. Chu, Y. Chen, J. Zhou, B. Zhou, J. Huang, Efficient and stable perovskite photodetectors based on thiocyanate-assisted film formation. *ACS Appl. Mater. Interfaces* **11**, 14510–14514 (2019).
46. Y. Chen, J. Zhang, J. Zhou, Y. Chu, B. Zhou, X. Wu, J. Huang, Long-term stable and tunable high-performance photodetectors based on perovskite microwires. *Adv. Opt. Mater.* **6**, 1800469 (2018).
47. W. Deng, X. Zhang, L. Huang, X. Xu, L. Wang, J. Wang, Q. Shang, S.-T. Lee, J. Jie, Aligned single-crystalline perovskite microwire arrays for high-performance flexible image sensors with long-term stability. *Adv. Mater.* **28**, 2201–2208 (2016).
48. H. Deng, X. Yang, D. Dong, B. Li, D. Yang, S. Yuan, K. Qiao, Y.-B. Cheng, J. Tang, H. Song, Flexible and semitransparent organolead triiodide perovskite network photodetector arrays with high stability. *Nano Lett.* **15**, 7963–7969 (2015).
49. H. Deng, D. Dong, K. Qiao, L. Bu, B. Li, D. Yang, H.-E. Wang, Y. Cheng, Z. Zhao, J. Tang, H. Song, Growth, patterning and alignment of organolead iodide perovskite nanowires for optoelectronic devices. *Nanoscale* **7**, 4163–4170 (2015).
50. L. Gu, M. M. Tavakoli, D. Zhang, Q. Zhang, A. Waleed, Y. Xiao, K.-H. Tsui, Y. Lin, L. Liao, J. Wang, Z. Fan, 3D arrays of 1024-pixel image sensors based on lead halide perovskite nanowires. *Adv. Mater.* **28**, 9713–9721 (2016).
51. Y. Liu, F. Li, C. Perumal Veeramalai, W. Chen, T. Guo, C. Wu, T. W. Kim, Inkjet-printed photodetector arrays based on hybrid perovskite $CH_3NH_3PbI_3$ microwires. *ACS Appl. Mater. Interfaces* **9**, 11662–11668 (2017).
52. S. Lim, M. Ha, Y. Lee, H. Ko, Large-area, solution-processed, hierarchical $MAPbI_3$ nanoribbon arrays for self-powered flexible photodetectors. *Adv. Opt. Mater.* **6**, 1800615 (2018).
53. L. Gao, K. Zeng, J. Guo, C. Ge, J. Du, Y. Zhao, C. Chen, H. Deng, Y. He, H. Song, G. Niu, J. Tang, Passivated single-crystalline $CH_3NH_3PbI_3$ nanowire photodetector with high detectivity and polarization sensitivity. *Nano Lett.* **16**, 7446–7454 (2016).
54. F. Cao, W. Tian, M. Wang, H. Cao, L. Li, Semitransparent, flexible, and self-powered photodetectors based on ferroelectricity-assisted perovskite nanowire arrays. *Adv. Funct. Mater.* **29**, 1901280 (2019).
55. D. Wu, H. Zhou, Z. Song, M. Zheng, R. Liu, X. Pan, H. Wan, J. Zhang, H. Wang, X. Li, H. Zeng, Welding perovskite nanowires for stable, sensitive, flexible photodetectors. *ACS Nano* **14**, 2777–2787 (2020).

Acknowledgments: We thank T. Liang at CAS Key Laboratory of Engineering Plastics, the Institute of Chemistry, Chinese Academy of Sciences, for the single-crystal XRD measurements, and B. Guan at Analysis and Testing Center, the Institute of Chemistry, Chinese Academy of Sciences, for the SAED measurements. **Funding:** This work was financial supported by the National Science Fund for Distinguished Young Scholars [grant nos. 22225502 (M.L.) and 52125302 (Q.C.)]; the National Natural Science Foundation of China [grant nos. 22435004 (M.L.), 22073107 (M.L.), 52321006 (Y.S.), 52350012 (Q.C.), and 22075009 (Q.C.)]; National Key R&D Program of China [grant nos. 2022YFE0202000 (M.L.) and 2021YFA0715700 (Q.C.)]; Bureau of International Cooperation, Chinese Academy of Sciences [grant no. 027GJHZ2022044MI (M.L.)]; and 111 Project [grant no. B14009 (L.J.)]. **Author contributions:** M.L. conceived and supervised the project. W.F., C.L., Z.Z., X.L., Q.S., and Y.W. performed the experiments and characterizations. W.F., C.L., C.W., Q.C., L.J., Y.S., and M.L. co-wrote the manuscript. All authors discussed the results and commented on the manuscript. **Competing interests:** The authors declare that they have no competing interests. **Data and materials availability:** All data needed to evaluate the conclusions in the paper are present in the paper and/or the Supplementary Materials.

Submitted 5 July 2024
Accepted 30 October 2024
Published 4 December 2024
10.1126/sciadv.adr5375

Downloaded from https://www.science.org at Imperial College London on December 10, 2024